Investigation of Erosion–Corrosion Resistance of Electroless Ni–P–Ti Composite Coatings

Zhi Li[1] · Md. Aminul Islam[2] · Zoheir Farhat[1]

Abstract

Electroless Ni–P–Ti composite coatings were prepared on AISI 1018 steel substrates by incorporating three different amounts of Ti nanoparticles into a Ni–P matrix. Erosion–corrosion tests were performed on AISI 1018 steel, Ni–P and Ni–P–Ti coatings. AISI 1018 steel exhibits the lowest erosion–corrosion resistance, while the highest erosion–corrosion resistance is achieved on coating containing 15.2 wt% Ti. For AISI 1018 steel, removal of oxide film by abrasive particles and severe pitting corrosion are the dominant erosion–corrosion mechanisms. For Ni–P coating, cracking and fracture of the coating are the prominent degradation mechanisms. However, micro-cutting, micro-ploughing and micro-indentation are the principal mechanisms for Ni–P–Ti coatings. Ti particles act as barriers during the erosion–corrosion process, which improve the erosion–corrosion resistance of the composite coatings.

Keywords Ni–P–Ti composite coating · Ti particles · Erosion–corrosion mechanisms · Synergistic effect

1 Introduction

Low carbon steel has been extensively used in automotive, oil and gas, and construction industries owing to their low cost and wide availability [1]. For example, in the oil and gas industry, pipelines, made of low carbon steel, are considered to be one of the most economical methods to transport petroleum products [2]. However, the erosion and corrosion resistance of steel pipelines is inadequate to withstand an aggressive environment [3]. The material degradation of pipelines prompted by erosion and corrosion has become a serious problem in the petroleum industry due to the presence of particulates (*i.e.* sands or other solid particles) and corrosive species (Cl$^-$, O_2, H_2S and CO_2) [4]. To protect the pipelines from erosion and corrosion, various preventative measures have been employed including different pipeline materials or protective coatings [5–7]. Nevertheless, using durable materials may not always be the most cost-effective solution [5]. Additionally, whilst the application of epoxy or polymer-based coatings have exhibited some improvement, each of these coatings have their limitations. Epoxy-based coatings are incapable of providing sufficient protection against certain chemicals in crude oil [6] and polymer-based coatings may suffer thermal damage during the assembly process [7], in addition to their low hardness. Therefore, there is still a demand for enhancement of these protective coatings to acquire a coating that imparts the highest protection to the pipelines devoid of frequent replacement or recoating procedure.

Electroless Ni–P has been widely utilized in many industries as protective coatings due to its high hardness, superior adhesion and exceptional corrosion resistance [8–10]. However, Ni–P coatings have low toughness and tend to crack readily under load or during impact [11]. Improved toughness can be achieved by adding ductile Ti particles into brittle matrix. Chu et al. reported that the fracture toughness of hydroxyapatite was improved by the addition of 20 vol% Ti particles [12]. Enrique et al. studied the effect of Ti nano-particles on the fracture toughness of Al_2O_3 based composite materials [13]. They found that fracture toughness is dependent on the Ti content and higher Ti content provides superior fracture toughness [13].

✉ Zhi Li
  Zhi.Li@dal.ca

1 Department of Mechanical Engineering, Dalhousie University, Halifax, NS B3J 2X4, Canada

2 Mining Wear and Corrosion Laboratory, National Research Council Canada, Vancouver, BC V6T 1W5, Canada

Jang et al. observed that Ti particles impart remarkable plasticity and toughness to the Mg-based bulk metallic glass composites and the compressive plasticity is enhanced from 12 to 25% strain by decreasing the mean Ti particle size from 89 ± 20 to 50 ± 17 μm [14]. In addition, Wang et al. found that the incorporation of Ti nanoparticles into Ni–P matrix can significantly improve toughness [2].

The erosion–corrosion resistance of Ni–P or Ni–P based composite coatings has been of considerable interest over the last two decades. For example, Ni–P–B_4C composite exhibits superior erosion–corrosion resistance in acidic chloride solutions at a normal abrasive impact compared to Ni–P coating [15]. Calderon et al. investigated the erosion–corrosion resistance of Ni–P–SiC composite coatings and suggested that the grain refining and microstructure changes caused by SiC particles contributed to the improved erosion–corrosion resistance [16]. More recently, Tamilarasan et al. studied the influence of reduced graphene oxide (rGO) on the erosion–corrosion behavior of Ni–P–rGO coatings and found that incorporation of rGO particles significantly improve the erosion–corrosion resistance and the best result is obtained at a concentration of 50 mg/L of rGO in the plating solution [3]. Although the aforementioned studies show improved erosion–corrosion resistance by incorporating third particles, the erosion–corrosion behavior of Ni–P–Ti coatings has not been studied.

The principal objective of this research is to investigate the erosion–corrosion behavior of AISI 1018 steel, Ni–P and Ni–P–Ti coatings. Different amount of Ti particles (1 g, 2 g, and 3 g) were separately added into Ni–P plating solutions. Pure corrosion, pure erosion, erosion enhanced corrosion and erosion–corrosion tests were conducted on AISI 1018 steel, Ni–P and Ni–P–Ti coatings with three different amounts of Ti content. This work examines the effects of Ti concentration on erosion–corrosion resistance. This study also identifies operative degradation mechanisms of different coatings during the erosion–corrosion process.

2 Experimental Details

2.1 Coating Preparation

AISI 1018 carbon steel coupons (18 mm × 10 mm × 6 mm) were utilized as substrates. The steel substrates were ground using various grit SiC papers (240, 320, 400, and 600). The ground substrates were then polished using diamond solutions (9 μm, 3 μm, and 1 μm).

Industrial grade Ni–P plating chemical solutions consisting of $NiSO_4$ as nickel source and $NaPO_2H_2$ as reductant were employed to prepare Ni–P–Ti plating solutions. 1 g, 2 g, and 3 g Ti particles were separately added into the Ni–P plating solutions (1 L volume). Figure 1 shows the particle size distribution of Ti powder. The Ti powder shows a bimodal size distribution. One is nano-size (approximately 40 nm), the other is micro-size (approximately 5 μm). Some particles are even larger than 10 μm. In order to avoid the oxidation of Ti particles, weighing and operating Ti powder were performed in a glovebox filled up with argon gas. The oxygen content in the glovebox was maintained at 0.1%. Ni–P plating solution without Ti particles was also prepared as pre-coating solution. The cleaning process of polished substrates comprised the removal of grease and debris by immersing in a heated alkali solution (85 °C) for 5 min, intermediate rinsing with distilled water and then followed by surface activation using 20 vol% sulfuric acid for 15 s. The alkali solution consists of 30 g/L Na_3PO_4, 30 g/L Na_2CO_3 and 50 g/L NaOH. Prior to submerging in the Ni–P pre-coating solution, the activated substrates were thoroughly rinsed with distilled water. To increase the adhesion strength of composite coatings, a thin Ni–P coating having a thickness of approximately 8 μm was deposited on the substrates. The coated samples were then hung in the Ni–P–Ti plating solutions. The electroless Ni–P–Ti plating parameters are summarized in Table 1. During plating, ammonium hydroxide was periodically added into a plating solution to adjust the pH. Ni–P coating without Ti particles was also
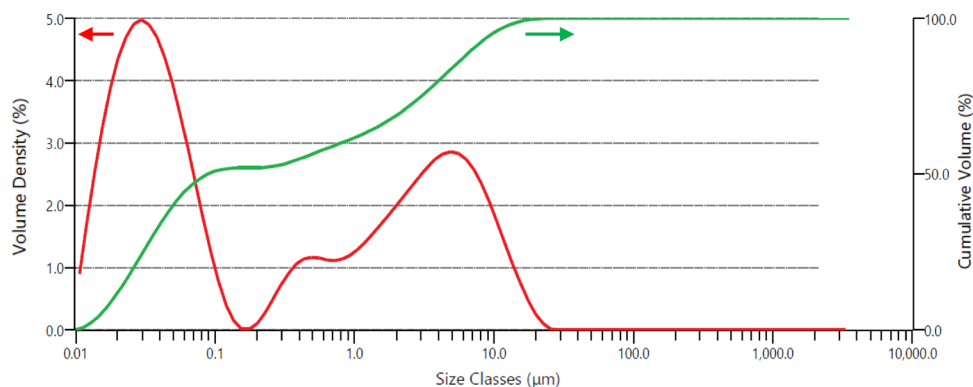
Fig. 1 Particle size distribution of Ti powder

Table 1 Electroless Ni–P–Ti plating parameters

Parameters	Values
Temperature	88 ± 2 °C
pH	4.7 ± 0.1
Magnetic stirring speed	300 rpm
Plating time	4–6 h

prepared for the comparative study. The plating time is dependent on the thickness of coatings containing different amounts of Ti. The coating thickness is approximately 50 μm.

2.2 Coating Characterization

The surface and cross-section of the coatings before and after erosion–corrosion tests were examined via scanning electron microscopy (SEM), energy dispersive spectrometry (EDS) and laser confocal microscopy. The operation conditions for SEM and EDS were 15 kV and 15 μA. A diamond pyramid indenter was employed to measure the Vickers hardness under 100 g load on the cross-sections of the coatings according to ASTM standard [17]. The diagonal lengths of indent were measured using an optical microscope for subsequent computation of hardness values.

2.3 Slurry Pot Erosion–Corrosion (SPEC) Test

Pure corrosion, pure erosion and erosion–corrosion tests were conducted on AISI 1018 steel, Ni–P and Ni–P–Ti coatings in a slurry pot erosion–corrosion (SPEC) tester. The schematic of the SPEC tester is shown in Fig. 2. The slurry was held in a glass container (4 L). An impeller driven by a motor was employed to impel the slurry.

Before the SPEC test, the specimen is cathodically protected during the test to provide material loss caused by pure erosion. Then except for the testing surface, other faces of the specimen were covered with epoxy. A test area of 1.8 cm^2 was exposed to the abrasive slurry. The abrasive slurry is composed of 35 wt% AFS 50–70 silica sand and 3.5 wt% sodium chloride solution. The SEM micrograph of AFS 50–70 angular silica sand particles is shown in Fig. 3. The average size of the abrasive particles ranges 200–300 μm. The impact velocity at an impeller speed of 900 rpm during erosion–corrosion testing process is measured to be in a range of 0.26–2.21 m/s [18]. The slurry temperature is approximately 45 °C and the testing time is 6 h. Pure erosion tests were conducted on samples without corrosion via cathodic protection. Pure corrosion tests (in the absence of abrasive particles) and erosion enhanced corrosion tests (in the presence of abrasive particles) under flowing conditions were conducted in a 3.5 wt% NaCl solution using the polarization resistance technique [19]. A three-electrode cell and a Gamry potentiostat were utilized
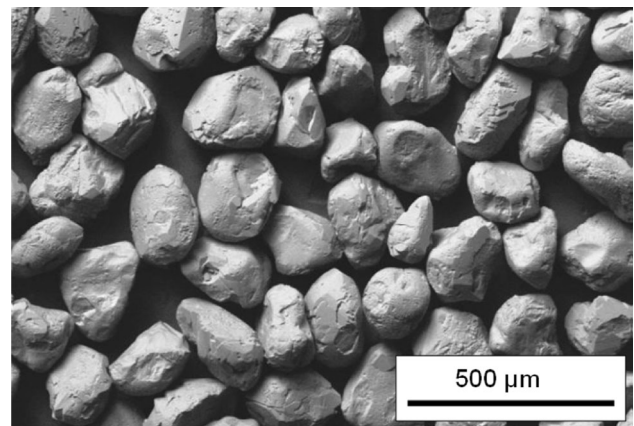
Fig. 3 SEM micrograph of AFS 50–70 abrasive sand particles

Fig. 2 Schematic of slurry pot erosion–corrosion tester
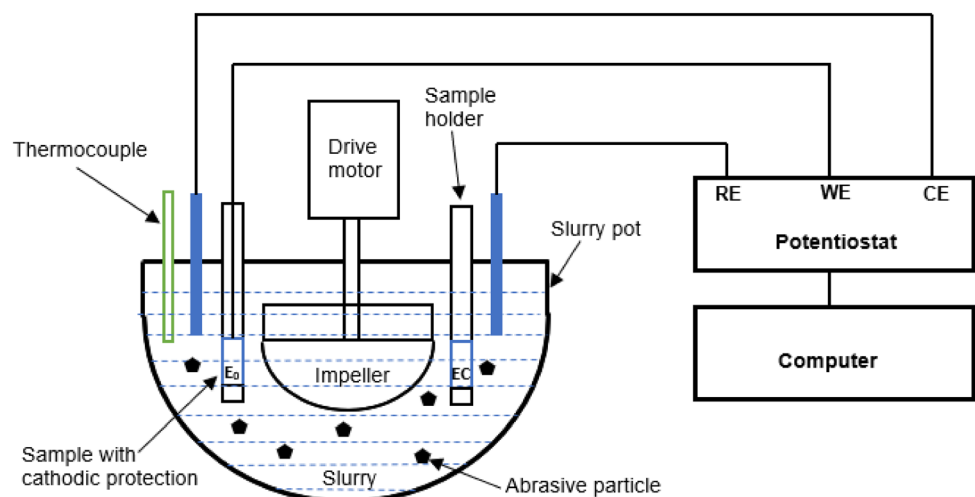
for electrochemical tests and cathodic protection [18]. A sample, a saturated calomel electrode (SCE), and platinum were used as a working electrode, a reference electrode, and a counter electrode in the three-electrode cell, respectively. A potential range from − 0.25 to + 0.25 V vs. the open circuit potential was employed with a scan rate of 0.167 mV/s. Each test was repeated twice to confirm the repeatability and the test results were averaged, the standard deviations were used as error bars.

A micro-balance having a reading accuracy of 0.01 mg was utilized to measure the mass loss after SPEC test. Material loss rate is reported as $cm^3/h/cm^2$. According to the ASTM G119-09, the total erosion–corrosion material loss rate (K_{ec}) can be expressd as follows [20]:

$$K_{ec} = K_{eo} + K_{co} + K_S \tag{1}$$

where, K_{eo} is the material loss rate caused by pure erosion, K_{co} is the material loss rate caused by pure corrosion and K_s is the material loss rate caused by synergy between erosion and corrosion. The total material loss rate, according to the ASTM G119-09, can be also expressed by the following components [20]:

$$K_{ec} = K_e + K_c = K_{eo} + K_{co} + \Delta K_e + \Delta K_c \tag{2}$$

where, K_e is the total erosion rate, K_c is the total corrosion rate, ΔK_e is the corrosion-enhanced erosion rate and ΔK_c is the erosion-enhanced corrosion rate. Combining Eqs. (1) and (2), the synergy material loss rate (K_s) and its components can be expressed as follows [20]:

$$K_s = \Delta K_e + \Delta K_c = K_{ec} - (K_{eo} + K_{co}) \tag{3}$$

$$\Delta K_c = K_c - K_{co} \tag{4}$$

$$\Delta K_e = K_s - \Delta K_c \tag{5}$$

3 Results

3.1 Coating Characterization

X-ray diffraction (XRD) analysis has been performed in our previous study [21]. XRD patterns revealed that all coatings consisted of amorphous Ni–P matrix, Ti peaks, and low TiO_2 peak associated with the as-received Ti powder [21]. The composition of coatings measured by EDS is given in Table 2. In the rest of the manuscript, Ni–P–Ti coatings are referred to as 5.1 wt% Ti, 11.8 wt% Ti and 15.2 wt% Ti (based on the Ti weight percent of the coatings).

Vickers hardness and Young's modulus of AISI 1018 steel and coatings at various Ti content is shown in Fig. 4. The error bar is the standard deviation of six indentations. Compared to AISI 1018 steel (Vickers hardness: 1.75

Table 2 Composition of Ni–P coating and Ni–P–Ti coating

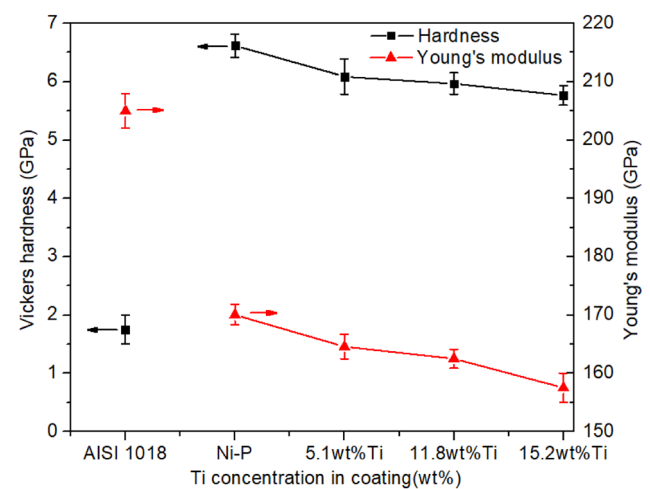| Coatings	Ni (wt%)	P (wt%)	Ti (wt%)
Ni–P	89.9	10.1	0.0
Ni–P–1gTi	86.0	8.9	5.1
Ni–P–2gTi	79.3	8.9	11.8
Ni–P–3gTi	78.1	6.7	15.2

Fig. 4 Vickers hardness and Young's modulus of AISI 1018 steel, Ni–P and Ni–P–Ti coatings

GPa), Ni–P and Ni–P–Ti coatings have much higher hardness. The Vickers hardness values of the coatings range from 5.7 to 6.7 GPa, which are in agreement with results measured by other researchers [22–24]. As the Ti content increases, the hardness of the coatings slightly decreases. This is mainly because Ti particles are softer (Vickers hardness 2–3 GPa [25]) than Ni–P matrix (Vickers hardness 5.7–7.0 GPa [22–24]), which lowers the overall hardness of the composite coatings [22]. The Young's moduli of the coatings have a similar trend as the Vickers hardness. As the Ti content increases, the Young's moduli decrease since the Ti particles have a lower young's modulus than the Ni–P coatings [22].

3.2 Corrosion Behavior

To study the pure corrosion resistance of AISI 1018 steel, Ni–P and Ni–P–Ti coatings, potentiodynamic polarization (PP) tests were conducted in 3.5 wt% sodium chloride solution (in the absence of abrasive particles) under flowing condition (900 rpm). Potentiodynamic polarization curves for tested samples are shown in Fig. 4. Compared to AISI 1018 steel, the potentiodynamic polarization curves of Ni–P and Ni–P–Ti coatings shift to a higher potential

position. The corrosion current density (i_{corr}) and corrosion potential (E_{corr}) were extracted from polarization curves using Tafel extrapolation. Corrosion rate (CR: mm/year) was calculated according to ASTM G102 [26]:

$$CR = \frac{i_{corr} \times EW}{D} \times 3.27 \times 10^{-3} \tag{6}$$

where, EW is the equivalent atomic weight, D is the density of the sample (g/cm^3), i_{corr} is expressed as μA/cm^2.

Table 3 shows corrosion characteristics of AISI 1018 steel, Ni–P and Ni–P–Ti coatings derived from polarization curves. Compared to AISI 1018 steel, Ni–P coating shows a much lower corrosion rate. The corrosion rate of Ni–P coating is approximately one-third of the AISI 1018 steel due to its amorphous structure and high concentration of phosphorus. The corrosion rates of Ni–P–Ti coatings are approximately one order of magnitude lower than that of Ni–P coating. As the Ti content increases, the corrosion rate of Ni–P–Ti coatings decreases, which indicates that the corrosion resistance is improved as the Ti content rises. This is mainly because of the ability of nano-Ti particles to fill the pores in the Ni–P matrix and the high tendency of nano-Ti particles to form an oxide layer [27–29]. Filling the pores in the Ni–P matrix lowers the overall porosity content of the Ni–P–Ti coatings and the oxide layer blocks the anodic–cathodic current passages, which in turn enhances the corrosion resistance of the Ni–P–Ti coatings [28].

To investigate the effects of abrasive particles on corrosion resistance, total corrosion rates were measured using potentiodynamic polarization (PP) technique in 3.5 wt% NaCl solution in the presence of abrasive particles under flowing condition (900 rpm). Figure 6 shows potentiodynamic polarization curves for tested samples in the presence of abrasive particles. The corrosion potential of Ni–P and Ni–P–Ti coatings is much higher than AISI 1018 steel, which indicates higher corrosion resistance in the presence of abrasive particles. Compared to the polarization curves of Ni–P–Ti coatings in the absence of abrasive particles (Fig. 5), the corrosion potential of the coatings in Fig. 6 are less noble due to the presence of abrasive particles. Tafel extrapolation was employed to extract the corrosion
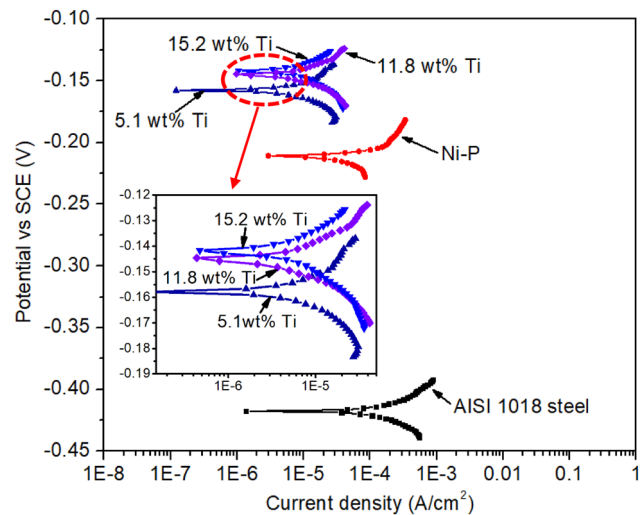
Fig. 5 Representative potentiodynamic polarization curves (in the absence of abrasive particle) for AISI 1018 steel, Ni–P and Ni–P–Ti coatings

potential (E_{corr}) and corrosion current density (i_{corr}) from potentiodynamic polarization curves. Corrosion rates were calculated using Eq. 6. Corrosion characteristics of AISI 1018 steel, Ni–P and Ni–P–Ti coatings are summarized in Table 4.

Total corrosion rates of AISI 1018 steel and Ni–P coating in presence of abrasive particles (Table 4) are approximately one order of magnitude higher than the pure corrosion rates in absence of abrasive particles (Table 5), while the difference in corrosion rates increases to two orders of magnitude for Ni–P–Ti coatings. In comparison with as-deposited Ni–P coating, as-deposited Ni–P–Ti coatings exhibit a much lower total corrosion rate. The total corrosion rates of as-deposited 5.1 wt% Ti, 11.8 wt%
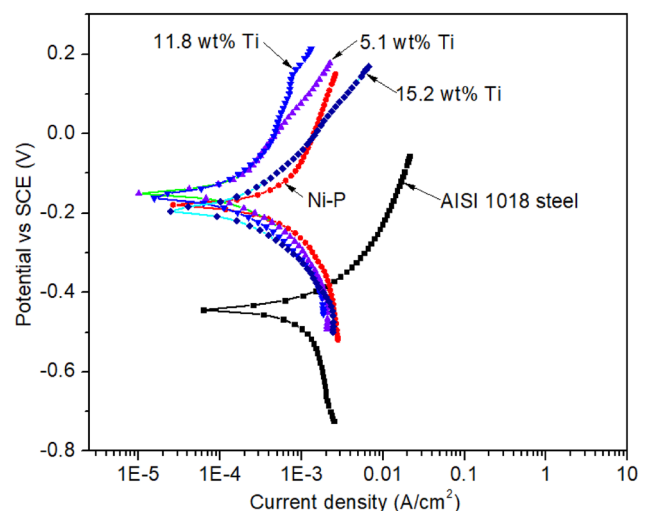
Table 3 Porosity density of coatings during pure corrosion

Samples	β_a (mV)	R_s or R_c (Ω cm^2)	P.D (%)
1018 steel	17.3 ± 1.9	44.6 ± 1.7	/
Ni–P	15.6 ± 1.7	129.9 ± 1.5	2.55 ± 0.05
5.1 wt%Ti	19.3 ± 1.5	895.4 ± 1.2	0.16 ± 0.03
11.8 wt% Ti	20.3 ± 1.2	922.6 ± 1.4	0.13 ± 0.02
15.2 wt% Ti	15.4 ± 1.3	988.7 ± 1.3	0.12 ± 0.03

Fig. 6 Potentiodynamic polarization curves (in the presence of abrasive particle) for AISI 1018 steel, Ni–P and Ni–P–Ti coatings

Table 4 Corrosion characteristics of samples derived from polarization curves in the presence of abrasive particles

Samples	E_{corr} (V)	i_{corr} (μA/cm^2)	CR (mm/year)
AISI 1018 steel	− 0.448 ± 0.005	800 ± 7	92.8 ± 0.6
Ni–P	− 0.169 ± 0.004	437 ± 5	49.6 ± 0.5
5.1 wt% Ti	− 0.136 ± 0.005	137 ± 3	12.9 ± 0.3
11.8 wt% Ti	− 0.146 ± 0.003	162 ± 2	14.7 ± 0.2
15.2 wt% Ti	− 0.170 ± 0.002	174 ± 3	16.7 ± 0.4

Table 5 Corrosion characteristics of tested samples derived from polarization curves in the absence of abrasive particles
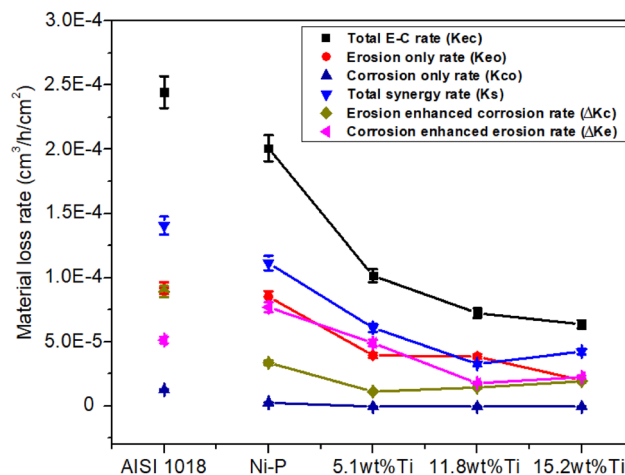
Samples	E_{corr} (V)	i_{corr} (μA/cm^2)	CR (mm/year)
AISI 1018 steel	− 0.415 ± 0.005	92.1 ± 0.7	10.70 ± 0.08
Ni–P	− 0.219 ± 0.004	33.1 ± 0.5	2.81 ± 0.05
5.1 wt% Ti	− 0.157 ± 0.007	4.8 ± 0.2	$4.21 ± 0.03 \times 10^{-1}$
11.8 wt% Ti	− 0.143 ± 0.002	4.5 ± 0.1	$4.11 ± 0.02 \times 10^{-1}$
15.2 wt% Ti	− 0.141 ± 0.003	3.4 ± 0.2	$3.24 ± 0.03 \times 10^{-1}$

Fig. 7 Material loss rate contribution of different components during erosion–corrosion

Ti, and 15.2 wt% Ti coatings are only 26.0%, 29.6%, and 33.7% of the as-deposited Ni–P coating, respectively. It is important to note that, in the presence of erosive particles, a slight decrease in corrosion resistance was observed as Ti content increases. Erosive particles remove passive films, which expose the fresh and more vulnerable surface to the corrosive solution [30, 31]. In the absence of abrasive particles, Ti particles exposed to the corrosive solution have a high tendency to form an oxide layer, which protects the coating from corrosion [27, 28]. However, in the presence of abrasive particles, as the Ti content increases, more TiO$_2$ layers are formed on the Ti particles' surface, which are then removed by abrasive particles, resulting in a higher corrosion rate.

3.3 Erosion–Corrosion Behavior

The total erosion–corrosion (E–C) rate (K_{ec}), erosion only rate (K_{eo}), corrosion only rate (K_{co}), total synergy rate (K_s), and the synergistic components (erosion-enhanced corrosion rate (ΔK_c) and corrosion–enhanced erosion rate (ΔK_e)) of AISI 1018, Ni–P and Ni–P–Ti coatings are displayed in Fig. 7.

Due to its higher hardness, Ni–P coating exhibits superior pure erosion resistance to AISI 1018 steel. Furthermore, the addition of Ti improves the pure erosion resistance. Although the hardness of Ni–P–Ti coatings slightly drops as Ti content increases, the toughness increases due to the ductile particle toughening [21]. Jang et al. suggested that the shear banding energy can be absorbed and the principal shear band can be brached into small shear bands by the dispersed ductile Ti particles, which in turn decreases stress concentration and improves toughness [32]. In our previous study, it was also found that the toughness of the Ni–P–Ti coatings is enhanced as Ti content increases. This increase in the toughness may improve the erosion resistance of the Ni–P–Ti coatings [21].

During erosion–corrosion, Ni–P coating displays a lower material loss rate than the AISI 1018 steel. On the other hand, the total erosion–corrosion rates of 5.1 wt% Ti, 11.8 wt% Ti and 15.2 wt% Ti coatings are only 50.7%, 36.3%, and 31.9% of that of Ni–P coating, respectively, suggesting that the total erosion–corrosion resistance improves with the increase in Ti content. The total erosion–corrosion resistance is dependent on pure corrosion, pure erosion, and synergy resistance. As the Ti content increases within the composite coatings, the total synergy rate and pure erosion rate decrease, which results in a lower total erosion–corrosion rate.

The total synergy rate decreases as Ti content increases up to 11.8 wt% which is then increased slightly when the Ti content is 15.2 wt%. Compared to pure erosion or pure corrosion, the synergistic effect is more complex. Synergy is composed of erosion enhanced corrosion and corrosion enhanced erosion contribution. It is worth noting that the corrosion enhanced erosion rate is much higher than the erosion enhanced corrosion rate, which suggests that corrosion enhanced erosion is dominant in the total synergy. Corrosion increases the surface roughness of the material. Erosion is highly dependent on the impact angle, which varies as the surface roughness increases, thus resulting in a higher erosion rate [31, 33]. As Ti content increases, more Ti particles fill the pores in the Ni–P matrix, which increases the impermeability of composite coatings and

thus improving the corrosion resistance. Besides, homogeneously dispersed Ti particles (with oxide layer) create uniformly distributed corrosion microcells, which produce a smoother surface compare to Ni–P coating. For Ni–P–Ti coating with 15.2 wt% Ti, both erosion enhanced corrosion and corrosion enhanced erosion are equally responsible for higher synergy contribution.

4 Discussion

4.1 Porosity Density

In order to study the corrosion mechanisms o composite coatings, the porosity density (P.D.) of the coatings based on polarization testing was estimated using the following equation [34]:

$$\text{P.D.} = \frac{R_s}{R_c} \times 10^{-\frac{\Delta E}{\beta_\alpha}} \tag{7}$$

where R_s is the polarization resistance of the 1018 steel substrate, R_c is the polarization resistance of the coated samples, ΔE is the corrosion potential difference between the 1018 steel substrate and the coated samples, and β_α is the slope of anodic Tafel extrapolation for the 1018 steel substrate.

Porosity density of coatings during pure corrosion derived from the Eq. (7) are summarized in Table 3. Ni–P coating has much higher porosity density due to the formation of hydrogen during the oxidation of $NaPO_2H_2$ in the electroless plating process [35]. The porosity density value of Ni–P coating is 2.55%, which is close to the value (2.40%) acquired in the study [29]. The porosity density of Ni–P–Ti coating is one order of magnitude lower than that of Ni–P coating. This is mainly because Ti nanoparticles can accommodate themselves to fit and fill the micro or nano-pores in the Ni–P matrix [29]. As the Ti content increases, more Ti particles fill the pores that result in lower porosity density. This explained why the corrosion resistance of Ni–P–Ti coatings improves with the increase in Ti content. Gheshlaghi et al. found that the corrosion resistance of Ni–P coating is considerably increased by the addition of WO_3 nanoparticles and suggested that the impermeability of the coating is improved by filling the pores with nanoparticles [36]. Allahkaram et al. calculated the porosity density of Ni–P-nanodiamond composite coatings and found that the porosity density decreases as the nanodiamond content increases within the coatings, which results in improved corrosion resistance [29]. The porosity density results are well consistent with the pure corrosion results (Table 5).

The porosity density of the coatings under erosion-enhanced corrosion derived from Eq. (7) are summarized in

Table 6 Porosity density of coatings during erosion enhanced corrosion

Samples	β_a (mV)	R_s or R_c ($\Omega\ cm^2$)	P.D (%)
1018 steel	141.6 ± 3.5	57.4 ± 5.5	/
Ni–P	501.9 ± 4.7	141.6 ± 4.3	29.01 ± 0.05
5.1 wt%Ti	284.1 ± 2.5	304.9 ± 5.9	11.96 ± 0.03
11.8 wt% Ti	217.7 ± 3.4	242.2 ± 3.6	12.33 ± 0.05
15.2 wt% Ti	241.5 ± 2.8	212.8 ± 5.2	13.04 ± 0.02

Table 6. Erosion enhanced corrosion exhibit much higher porosity density than pure corrosion (Table 3). The impacts of abrasive particles cause a high strain layer on the coating surface, which is more anodic and highly vulnerable to corrosion [30]. During the corrosion process, a layer of protective oxide film is formed. The abrasive particles break the oxide film and expose the fresh surface to the corrosive environment. Due to the breakdown of the protective film, pits are initiated at the surface, which increase the porosity density. Compared to Ni–P coating, Ni–P–Ti coatings have much lower porosity density due to their higher erosion resistance. As the Ti content increases, the porosity density of the composite coatings increases slightly, which is consistent with the total corrosion results presented in Table 4.

4.2 Anti-Corrosion Mechanisms

Ni–P coating exhibits a much lower pure corrosion rate than AISI 1018 steel (Table 5). Several reasons may contribute to this exceptional corrosion resistance. First, Ni–P amorphous coating exhibits superior corrosion resistance relative to the crystalline counterparts due to the absence of grains and grain boundaries [37]. Secondly, the dissolution rate of P is much lower than that of Ni, resulting in an enrichment of the elemental P surface [38]. This phosphorus-enriched layer functions as a barrier that blocks the primary dissolution sites and prohibits the anodic dissolution [38]. Third, as the dissolution process advances, the enriched phosphorus in the surface reacts with water to form hypophosphite anions [39]. These hypophosphite anions are absorbed on the coating surface, which shields the coating surface from water, prevents the formation of nickel hydrate, hinders the anodic dissolution of Ni and eventually passivates the coating surface [28, 38]. In addition, the highly reducing nature of the hypophosphite anions may help prevent the dissolution of Ni [38]. Lastly, Ching [40] observed that phosphorus can function as an acceptor that is capable of receiving approximately 0.6 electrons from Ni in a Ni–20P alloy. Diegle et al. [38] proposed that this donor–acceptor behavior may improve

the activation energy for the anodic dissolution of Ni, which results in enhanced corrosion resistance of the Ni-20P amorphous alloy. Furthermore, the formation of passive film (NiO) on coating surface under flowing condition may also contribute to the high corrosion resistance [41].

The corrosion rates of the as-deposited Ni–P–Ti coatings are much lower than that of the Ni–P coating and the lowest corrosion rate is achieved on the 15.2 wt% Ti coating (Table 5). Several anti-corrosion mechanisms are proposed to explain the enhancement of the corrosion resistance of Ni–P-based composite coatings in comparison with Ni–P coating. Abdel [42] studied the corrosion resistance of Ni–TiO_2 composite coating and indicated that TiO_2 particles play a pivotal role in enhancing the corrosion resistance. Firstly, the inert TiO_2 particles act as barriers to refine the microstructure of the Ni matrix during deposition, thereby lowering the corrosion rate [42]. Secondly, the homogeneously dispersed TiO_2 particles prevent localized corrosion by producing uniformly distributed corrosion micro cells [42]. In the present study, Ti particles were incorporated in the Ni–P matrix. Ti nanoparticles exhibit a high tendency to form a TiO_2 layer on the surface [27, 28]. Therefore, the anti-corrosion mechanisms proposed by Abdel [42] could be employed to explain the improved corrosion resistance of Ni–P–Ti coatings. In addition, it is believed that nanoparticles can accommodate themselves to fill the nano and micropores in the Ni–P matrix, thus improving the impermeability of the coatings [29]. From Table 3, it is observed that the porosity density of Ni–P–Ti coatings is much lower than that of Ni–P coating and the lowest porosity density is reached on 15.2 wt% Ti coating that possesses the highest corrosion resistance. Hence, considering the anti-corrosion mechanisms discussed above, superior corrosion resistance of Ni–P–Ti coatings may be due to the formation of TiO_2 layer, barrier effect and decreased porosity density.

4.3 Erosion–Corrosion Mechanisms

To investigate the erosion–corrosion mechanisms, the AISI 1018 steel samples' surface before and after erosion–corrosion for 30 min was examined using SEM and EDS. Based on EDS results, it is confirmed that iron oxide (Fe_xO_y) layer (at.% of Fe: 33%, at.% of O: 67%) is formed on the surface after erosion–corrosion test (Fig. 8). Figure 9a shows the optical micrograph of AISI 1018 steel before erosion-erosion. It is observed that the surface is smooth and flat. After erosion–corrosion, severe surface degradation is observed (Fig. 9b, c and d). During erosion–corrosion, an oxide layer is formed on the AISI 1018 steel surface due to corrosion. As the thickness of the oxide layer increases, it becomes brittle. This brittle oxide layer then undergoes cracking and fracture due to abrasive particle impact (Fig. 9c and d). The removal of the oxide layer exposes the fresh iron surface to corrosion, which accelerates the material loss rate.

Figure 10a shows the surface morphology of Ni–P coating before erosion–corrosion test. A nodular structure and pores are observed on the coating surface. Figure 10b–d show the SEM micrographs of Ni–P coating after erosion–corrosion (for 30 min). Abrasive particle impact results in cracking and fracture due to the low toughness of the coating (Fig. 10b). The fracture fragments were then removed by the following erosive particles, creating cavities. These cavities are extremely vulnerable to localized corrosion. Scratching by the sharp edge of abrasive particles causes cracking and fracture on the coating surface (Fig. 10c and d). There is also some evidence of pitting on the scratch scar (Fig. 10c) due to the high strain (more anodic). For Ni–P coating, cracking and fracture caused by the abrasive particles are the dominant wear mechanisms. Localized corrosion at degraded sites is the governing corrosion mechanism during erosion–corrosion.

SEM micrograph of 15.2 wt% Ti coating before erosion–corrosion test is shown in Fig. 11a. Compared to Ni–P coating (Fig. 10a), 15.2 wt% Ti coating contains a more refined nodular structure and a denser surface. Because of its homogenously distributed Ti particles, 15.2 wt% Ti coating undergoes uniform degradation during erosion–corrosion (Fig. 11b). Due to its improved toughness, micro-ploughing, low angle micro-cutting, plastic deformation and micro-scratching caused by the abrasive particles are the dominant wear mechanisms. During ploughing, abrasive particle pushes the material to the sides and in front of its sliding direction (Fig. 11c and e). The heavily strained material at the rim or at the end of the ploughing scar is then removed by subsequent impacts. During low angle micro-cutting (Fig. 11d), an angular particle moves forwards, indenting the surface and cuts a small portion of material. In some cases, the corrosive solution penetrates the subsurface layer through the microfracture or microcracks, which corrodes the subsurface layer. Then the unsupported top layer is removed by the subsequent impacts causing spallation (Fig. 11f).

To further study the erosion–corrosion mechanisms of AISI 1018, Ni–P and Ni–P–Ti coatings, the cross-sections of samples after erosion–corrosion were examined under optical microscopy and SEM. Figure 12 shows the cross-sections of different samples after erosion–corrosion for 30 min. From Fig. 12a, it is observed that AISI 1018 steel undergoes severe pitting corrosion. Figure 12b shows the EDS map of one pit, the green color represents iron and the red color is oxygen. EDS confirms that the oxidation product (EDS results: at.% of Fe: 33%, at.% of O: 67%) is formed, which undergoes cracking and fracture (Fig. 12c and d). For AISI 1018 steel, an oxide film (thickness:
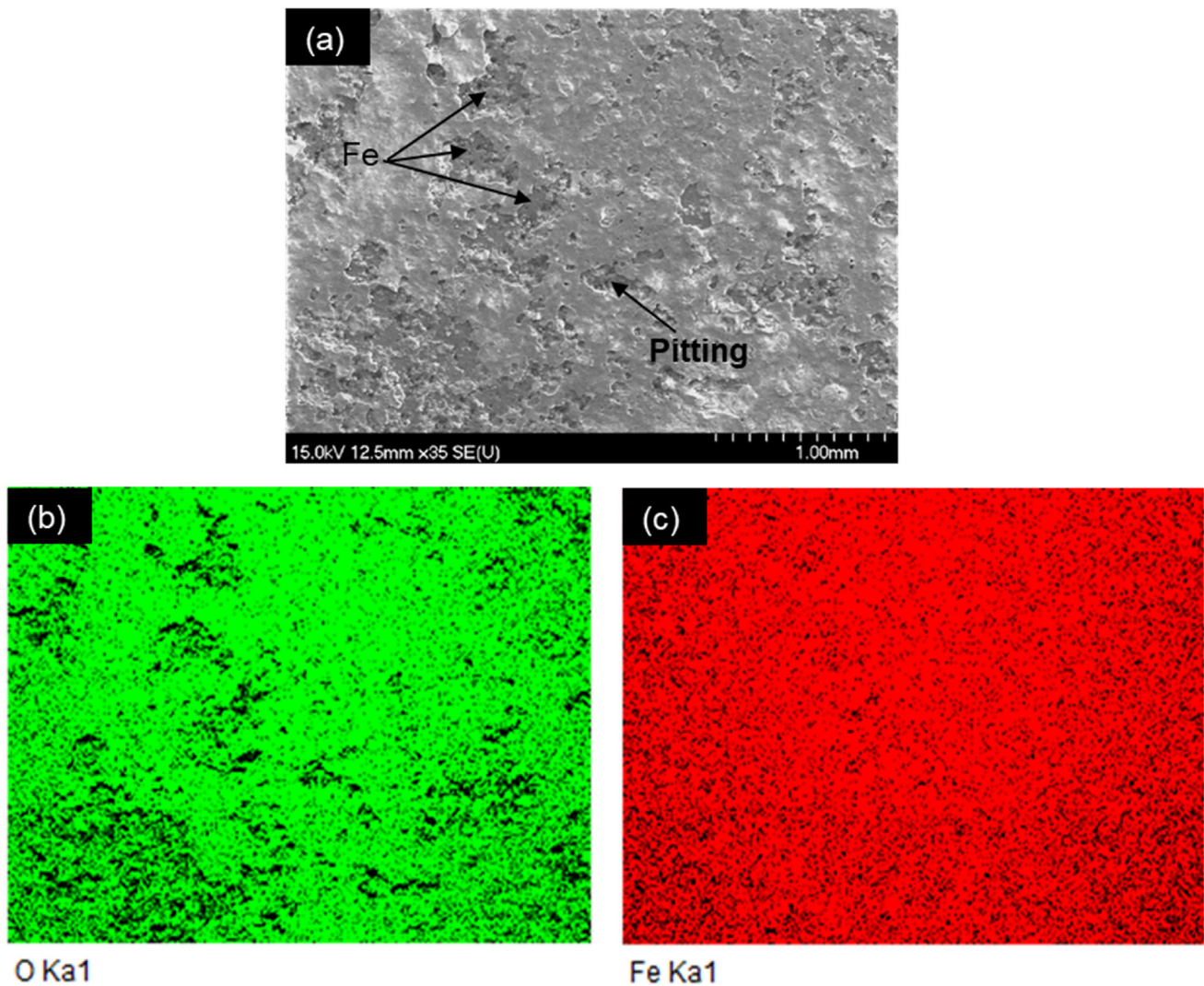
Fig. 8 **a** SEM micrograph, **b** and **c** corresponding EDS element maps of AISI 1018 steel after erosion–corrosion for 30 min

2–3 μm) is formed on the surface, which is then removed by abrasive particle impact. Due to the breakdown of the oxide film, pits initiate at the surface. These pits continue to grow and are filled with corrosion products. Because of the brittle nature of the corrosion product, it is then removed easily and contributes to the total material loss rate.

The cross-section micrograph of Ni–P coating is shown in Fig. 12e. The insets are the magnified micrographs of marked parts. Abrasive particle impact causes cracking of the coating. These cracks propagate to the subsurface of the coating which results in the fracture of the coating. Then the following impacts remove the fracture deris and cause material loss (Fig. 12e). Therefore, cracking and fracture are the dominant material removal mechanisms for the Ni–P coating. On the other hand, after 30 min erosion–corrosion, the thickness of 15.2 wt% Ti coating is uniform, no cracks or fracture is observed on cross-section (Fig. 12f).

This suggests that 15.2 wt% Ti coating undergoes uniform material degradation and has higher toughness compared to Ni–P coating. Micro-indentation or localized material removal (micro-cutting and micro-ploughing) is observed on the cross-section (Fig. 12g). No microcracks are present in the vicinity of indent even at high magnification (20 K times) due to the ductile Ti particle toughening (Fig. 12h). During erosion–corrosion, micro-cracking and fracture contribute to a higher material loss for Ni–P coating, whereas Ni–P–Ti coatings undergo ductile material degradation with lower material loss due to improved toughness.

To investigate the role of Ti particles during erosion–corrosion, examinations of 15.2 wt% Ti coating surface using SEM and EDS element maps were performed after erosion–corrosion. Figure 13a shows the SEM micrograph of 15.2 wt% Ti coating after erosion–corrosion for 30 min. Corresponding EDS element maps are given in Fig. 13b–e.
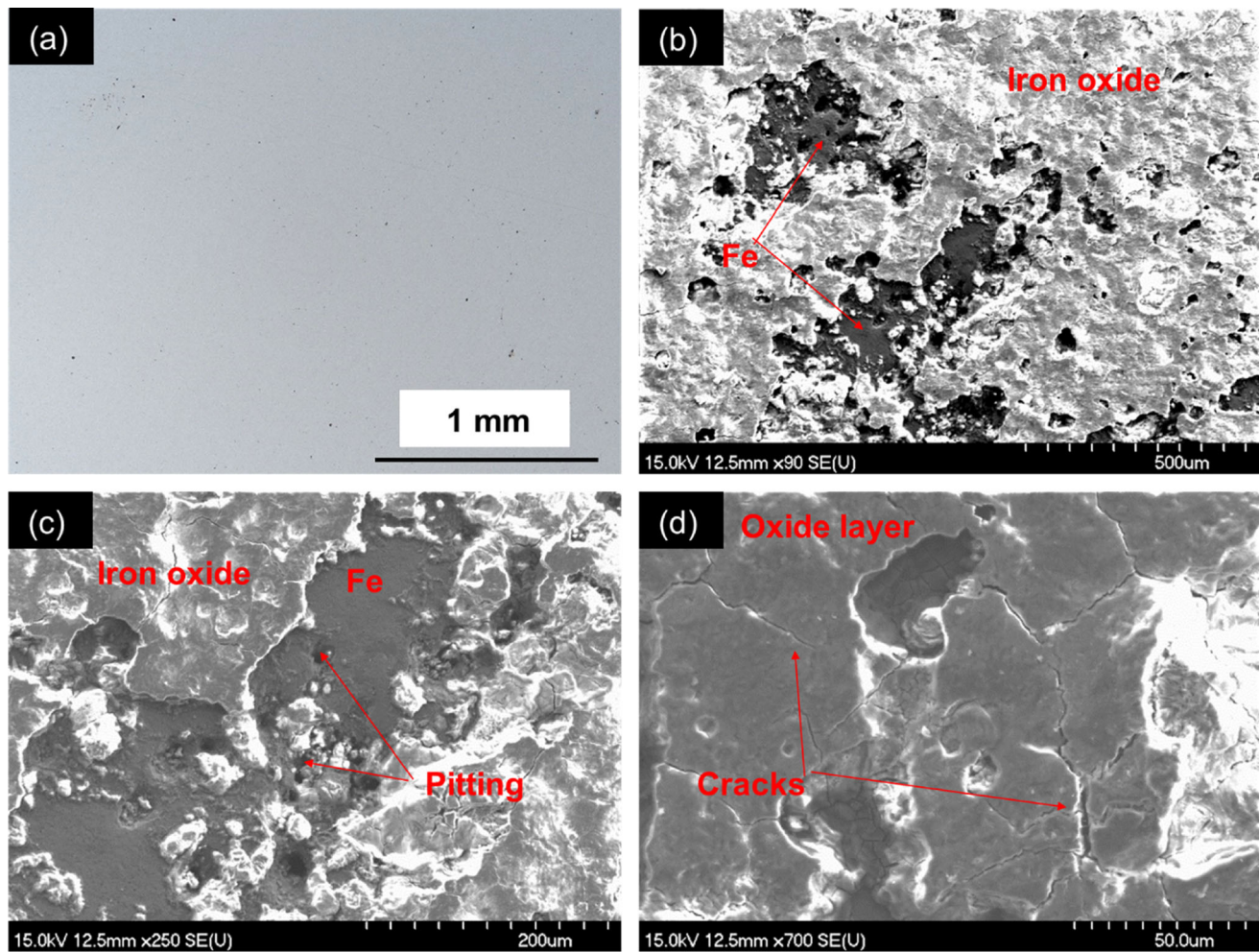
Fig. 9 **a** optical micrograph of AISI 1018 steel before erosion–corrosion and **b**, **c**, **d** SEM micrographs of AISI 1018 steel after erosion–corrosion for 30 min

It is important to note that Ti particles are uniformly distributed in the Ni–P matrix. Oxygen was detected on the coating surface after erosion–corrosion, which suggests that an oxide layer is formed on the surface. Es-Souni et al. [27] proposed that titanium and titanium alloys exhibit a high tendency to form a layer of TiO_2 on the surface. Fayyad et al. [28] also confirmed the formation of titanium oxide on the surface of NiTi nanoparticles.

SEM micrographs in Fig. 14 illustrates the effects of Ti particles on various material removal processes. Ti particle acts as a barrier in front of the sliding abrasive particle. As observed in Fig. 14a, the micro-scratching path is deflected by the Ti particle. when an abrasive particle slides over a Ti particle during micro-ploughing (Fig. 14b) or micro-cutting (Fig. 14f), the kinetic energy of the abrasive particle is absorbed by the Ti particle through elastic or plastic deformation. The abrasive particle loses the kinetic energy, which results in a significant reduction in driving force for micro-ploughing or micro-cutting. Ultimately, the micro-

ploughing or micro-cutting is impeded by the Ti particle. On the other hand, when an abrasive particle impacts the interface of Ti particle and Ni matrix at a normal angle (Fig. 14c), the matrix is deformed, whereas the ductile core of Ti particle absorbs the impact energy and the Ti particle remains intact. Therefore, the impact is restricted by the Ti particle. Figure 14d shows the material in the vicinity of a Ti particle is removed by micro-cutting, whereas the Ti particle remains intact. This suggests that the Ti particle is more wear-resistant than the matrix. When an abrasive particle impacts a Ti particle (Fig. 14e), the Ti particle functions as a barrier and consumes the kinetic energy of the abrasive particle. The ductile core of Ti particles provides high toughness, which is capable of absorbing the impact energy of abrasive particles without cracking and fracture.

In the present study, as the Ti concentration (weight percent) increases within the composite coatings, the volume fraction of Ti particles increases, which reduces the
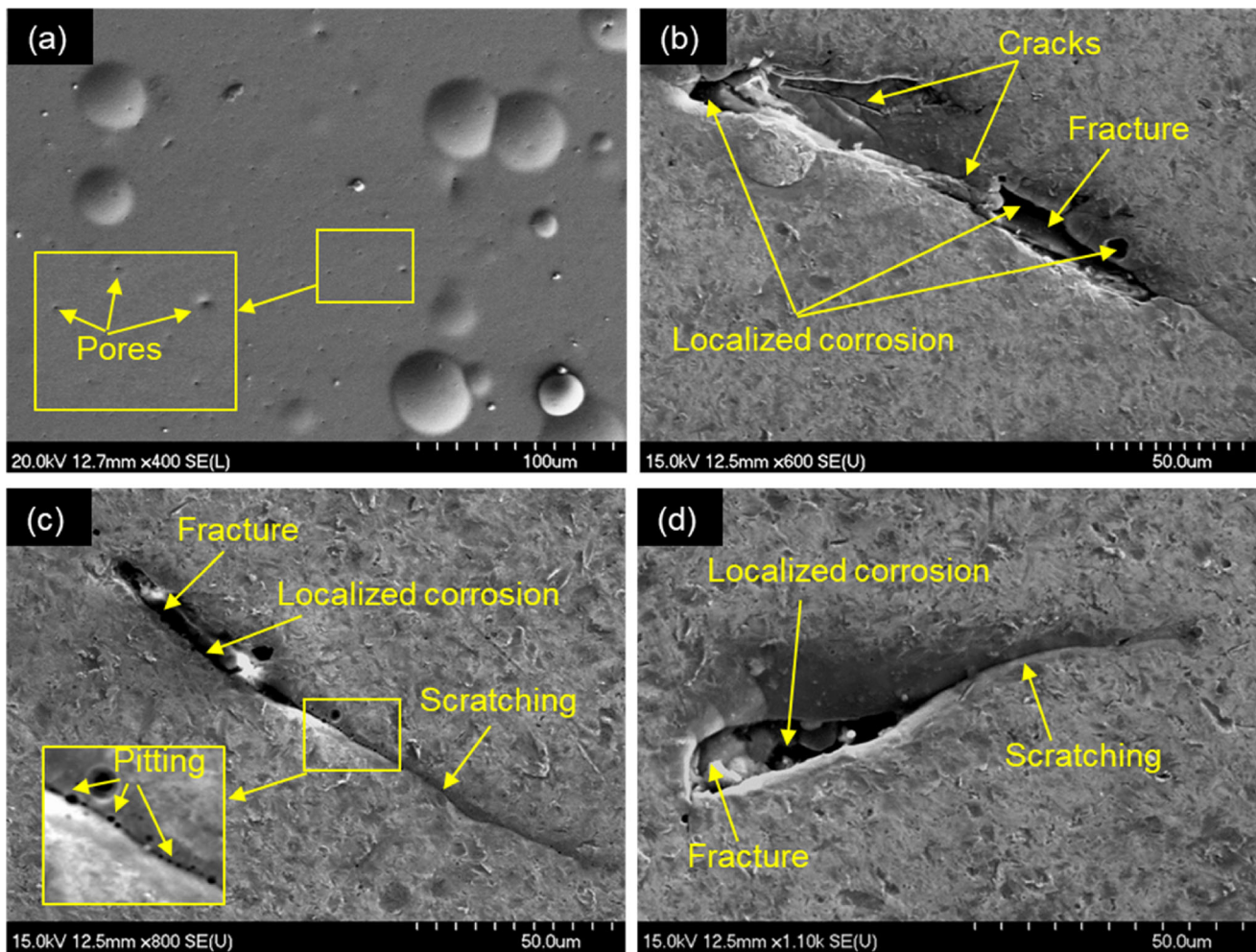
Fig. 10 SEM micrographs of **a** Ni–P coating before and **b**, **c**, **d** after erosion–corrosion for 30 min

interparticle spacing between Ti particles. The reduction in interparticle spacing makes the barrier effects more effective. This explains the changes in erosion–corrosion mechanisms of 15.2 wt% Ti coating compared to Ni–P coating. For Ni–P coating, due to its low toughness; fracture and cracking are the main erosion–corrosion mechanisms, which cause high material loss rate. On the other hand, for Ni–P–Ti composite coating; micro-ploughing, micro-cutting and plastic deformation are the dominant erosion–corrosion mechanisms, which provides a uniform material degradation and low material loss rate.

In addition, formation of the oxide layer (TiO_2) on the Ti particle surface may improve the erosion–corrosion resistance. TiO_2 has a high hardness (8–11GPa) [43, 44] and inert nature, which not only improves the erosion resistance but also enhances the corrosion resistance of composite coatings. Chen and Gao found that Ni–TiO_2 and Ni–P–TiO_2 coatings possess much

higher hardness and scratch resistance in comparison with Ni and Ni–P coatings, respectively [45]. Uysal studied the tribological and corrosion behavior of Ni–P and Ni–P–TiO_2 coatings and found that both wear and corrosion resistance are enhanced by incorporation of TiO_2 into Ni–P matrix due to the high hardness and inert nature of TiO_2 [46].

The dominant erosion–corrosion mechanisms for different materials are given in Table 7. In summary, corrosion film removal by abrasive particles and severe pitting corrosion are the main material removal mechanisms for AISI 1018 steel. On the other hand, the addition of Ti particles into Ni–P matrix improves the coating's toughness, which changes the erosion from a brittle (cracking and fracture for Ni–P coating) to a ductile (micro-cutting and micro-ploughing for Ni–P–Ti coatings) material removal mechanism. In addition, formation of an oxide layer on Ti particles improves both the erosion and corrosion resistance of Ni–P–Ti coatings. Ti particles have a
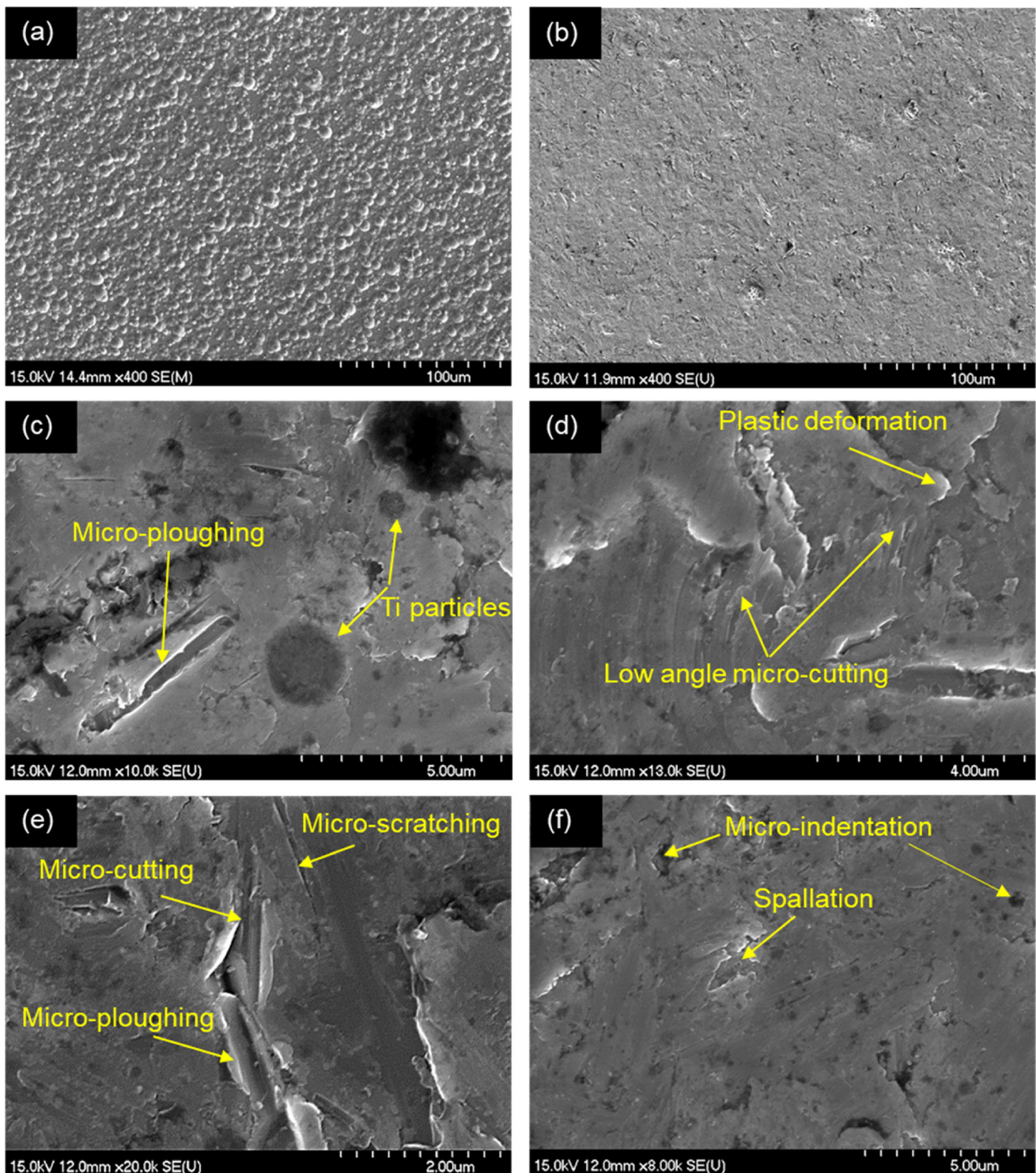
Fig. 11 SEM micrographs of **a** 15.2 wt% Ti coating before and **b–f** after erosion–corrosion for 30 min

ductile core and a hard oxide surface layer. The ductile core can absorb the kinetic energy of the abrasive particles and the hard surface layer has high wear and corrosion resistance. This makes the Ti particles function as barriers to both wear and corrosion.

5 Conclusion

Ni–P and Ni–P–Ti coatings were deposited on AISI 1018 steel using electroless plating. Erosion–corrosion resistance of AISI 1018 steel, Ni–P and Ni–P–Ti coatings was
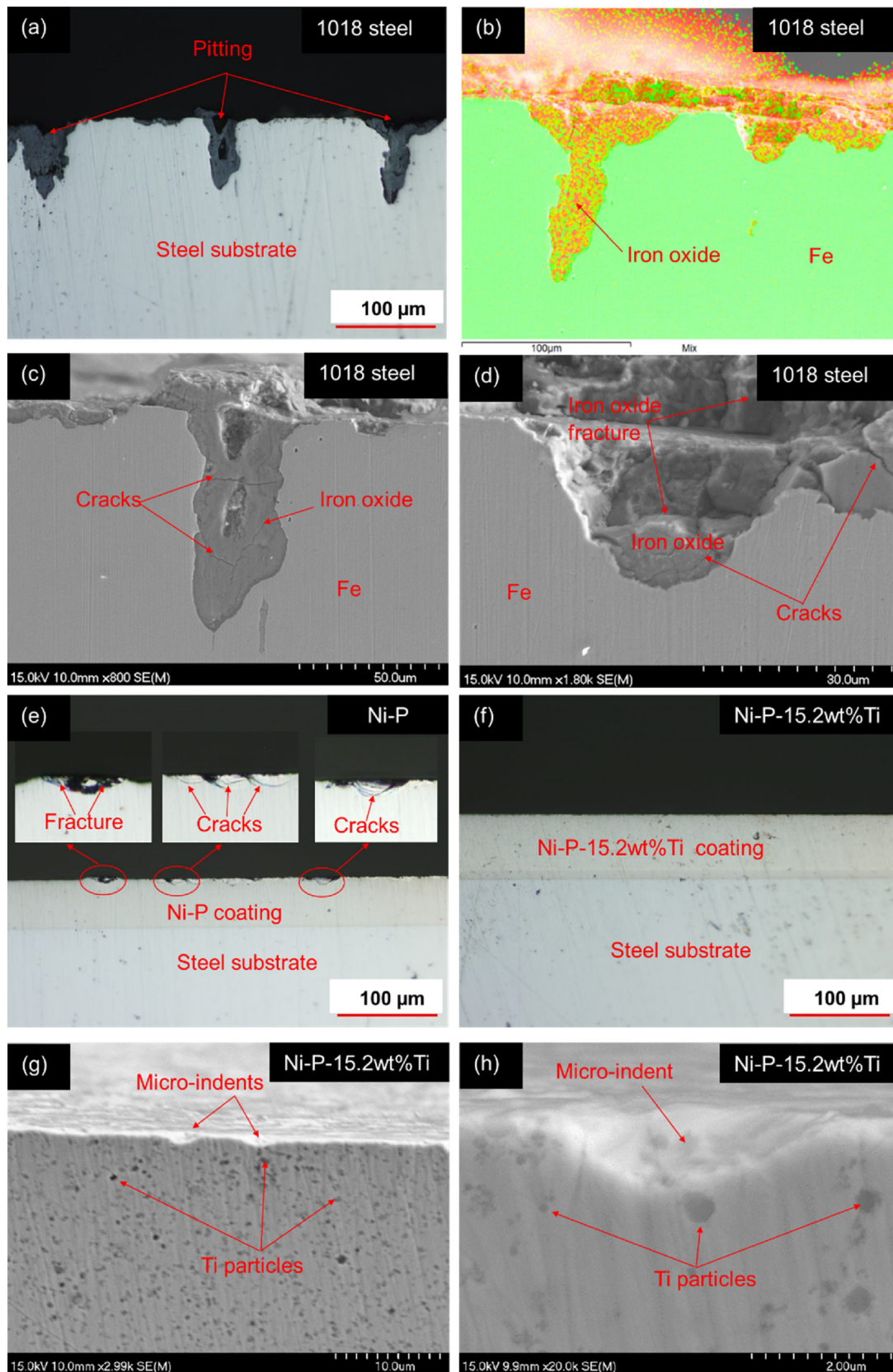
Fig. 12 a optical cross-section micrograph of 1018 steel; **b** EDS cross-section map of 1018 steel; **c, d** SEM cross-section micrographs of 1018 steel; **e** optical cross-section micrograph of Ni–P coating; **f** optical cross-section micrograph of Ni–P–15.2wt% Ti coating; **g, h** SEM cross-section micrographs of Ni–P–15.2wt% Ti coating
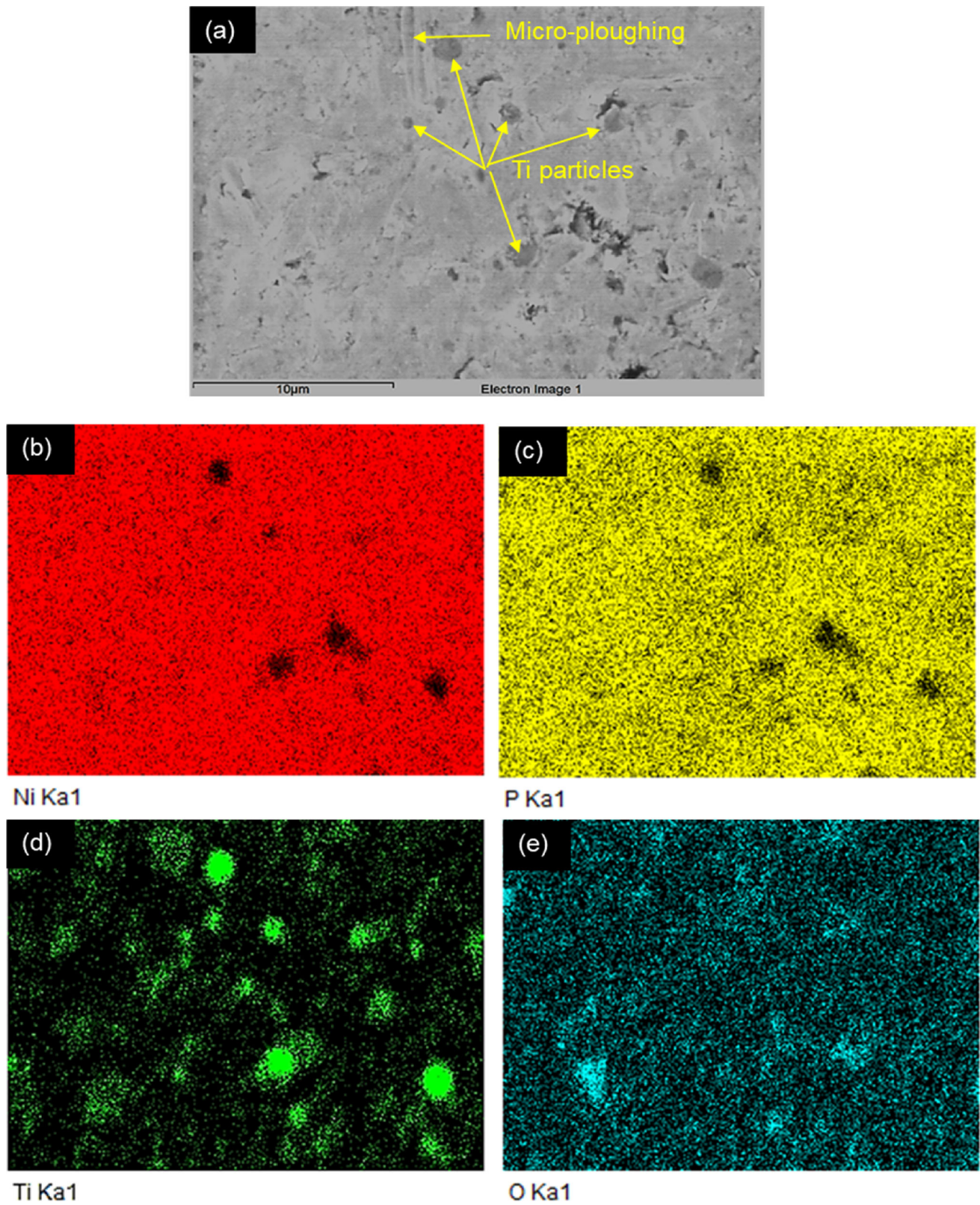
Fig. 13 **a** SEM micrograph, and **b–e** EDS element maps of 15.2 wt% Ti coating after erosion–corrosion for 30 min
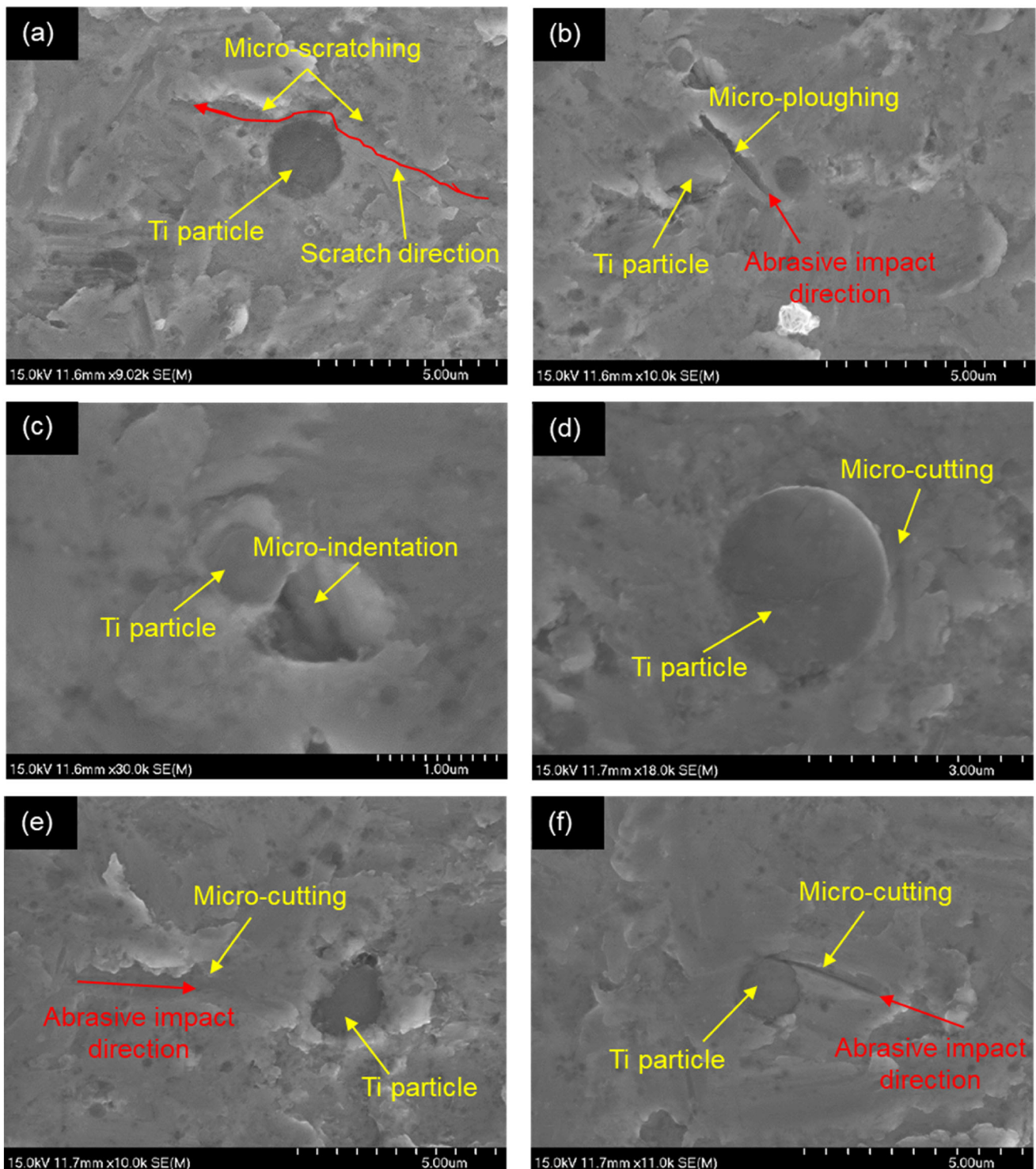
Fig. 14 SEM micrographs of interactions between Ti particles and various material removal mechanisms

assessed using slurry pot erosion–corrosion. Several conclusions can be obtained from the present work:

1. Compared to Ni–P coating, Ni–P–Ti coatings show higher corrosion resistance due to their lower porosity density and formation of TiO_2 surface layer on Ti particles.

2. Ni–P–Ti coatings exhibit superior pure erosion resistance in comparison with Ni–P coating due to their improved toughness.

Table 7 Summary of dominant erosion–corrosion mechanisms

Materials	Dominant erosion–corrosion mechanisms
AISI 1018 steel	Corrosion film removal by abrasive particles
	Severe pitting corrosion
Ni–P coating	Cracking and fracture of coating
	Localized corrosion at cracking and fracture sites
Ni–P–Ti coating	Micro-ploughing
	Micro-cutting
	Micro-scratching
	Micro-indentation
	uniform corrosion
	Ti particles act as barriers to prevent micro-ploughing, micro-cutting, micro-indentation and micro-scratching

3. AISI 1018 steel has the lowest erosion–corrosion resistance, whereas 15.2 wt% Ti coating exhibits the optimal erosion–corrosion resistance. The erosion–corrosion resistance of Ni–P–Ti coatings increases as Ti content rises.

4. SEM observation revels that, pitting and removal of the corrosion layer by abrasive particle impact are the dominant erosion–corrosion mechanisms for AISI 1018 steel. Cracking and fracture are the main mechanisms for Ni–P coating. For Ni–P–Ti coatings, micro-cutting, micro-ploughing and micro-scratching are the predominant mechanisms.

5. Ti particles serve as barriers for micro-cutting, micro-ploughing, micro-indentation as well as corrosion, which significantly enhance the erosion–corrosion resistance of Ni–P–Ti coatings.

Compliance with Ethical Standards

Conflict of interest On behalf of all authors, the corresponding author states that there is no conflict of interest.

References

1. Gandy D (2007) Carbon steel handbook. Electric Power Research Institute, Washington, pp 1–172
2. Wang C, Farhat Z, Jarjoura G, Hassan MK, Abdullah AM (2018) Indentation and bending behavior of electroless Ni–P–Ti composite coatings on pipeline steel. Surf Coat Technol 334:243–252
3. Tamilarasan TR, Sanjith U, Shankar MS, Rajagopal G (2017) Effect of reduced graphene oxide (rGO) on corrosion and erosion–corrosion behaviour of electroless Ni–P coatings. Wear 390–391:385–391
4. MacLean M, Farhat Z, Jarjoura G, Fayyad E, Abdullah A, Hassan M (2019) Fabrication and investigation of the scratch and indentation behaviour of new generation Ni–P-nano-NiTi composite coating for oil and gas pipelines. Wear 426–427:265–276
5. Wang C (2017) Indentation and fracture behaviour of electroless Ni–P-based composite coatings. Dalhousie University, Halifax
6. Bayram TC, Orbey N, Adhikari RY, Tuominen M (2015) FP-based formulations as protective coatings in oil/gas pipelines. Prog Org Coat 88:54–63
7. Taubkin IS, Sukhov AV, Rudakova TA (2004) Analysis of the behavior of a protective polymer coating for gas pipelines under the action of applied heat. Plast Massy 6:31–37
8. Vojtěch D, Novák M, Zelinková M, Novák P, Michalcová A, Fabián T (2009) Structural evolution of electroless Ni–P coating on Al–12wt.% Si alloy during heat treatment at high temperatures. Appl Surf Sci 255:3745–3751
9. Lee CK (2009) Electrochemical and wear-corrosion properties of electroless nickel–phosphorus deposition on CFRP composites. Mater Chem Phys 114:125–133
10. Xu XQ, Miao J, Bai ZQ, Feng YR, Ma QR, Zhao WZ (2012) The corrosion behavior of electroless Ni–P coating in Cl−/H2S environment. Appl Surf Sci 258:8802–8806
11. Wang C, Farhat Z, Jarjoura G, Hassan MK, Abdullah AM (2017) Indentation and erosion behavior of electroless Ni–P coating on pipeline steel. Wear 376–377:1630–1639
12. Chu C, Lin P, Dong Y, Xue X, Zhu J, Yin Z (2002) Farbrication and characterization of hydroxyapatite reinforced with 20 vol% Ti particles for use as hard tissue replacement. J Mater Sci 13:985–992
13. Enrique RR, José RG, Sergio EV, Brianda CS, Ivanovich EG, Roberto MS (2016) Effect of particle size and titanium content on the fracture toughness of particle-ceramic composites. Mater Today 3:249–257
14. Jang JSC, Li JB, Lee SL, Chang YS, Jian SR, Huang JC, Nieh TG (2012) Prominent plasticity of Mg-based bulk metallic glass composites by ex-situ spherical Ti particles. Intermetallics 30:25–29
15. Bozzini B, Cavallotti PL, Parisi G (2013) Corrosion and erosion–corrosion of electrodeposited Ni–P/B4C composites. Br Corros J 36:49–55
16. Calderón JA, Henao JE, Gómez MA (2014) Erosion–corrosion resistance of Ni composite coatings with embedded SiC nanoparticles. Electrochim Acta 124:190–198
17. ASTM (2015) Standard test method for vickers indentation hardness of advanced ceramics. ASTM Internatinal, Conshohocken
18. Islam MA, Jiang J, Xie Y, Fiala P (2017) Investigation of erosion–corrosion behavior of (WTi)C based weld overlays. Wear 390–391:155–165
19. ASTM (2014) Standard test method for conducting potentiodynamic polarization resistance measurements. ASTM Internatinal, Conshohocken
20. ASTM (2009) Standard guide for determining synergism between wear and corrosion. ASTM Internatinal, Conshohocken
21. Li Z, Farhat ZN, Jarjoura G, Fayyad E, Abdullah A, Hassan M (2019) Synthesis and characterization of scratch resistant Ni–P–Ti based composite coating. Tribol Trans 62:880–896
22. Balaraju JN, Narayanan TSNS, Seshadri SK (2003) Electroless Ni–P composite coatings. J Appl Electrochem 33:807–816
23. Sahoo P, Das SK (2011) Tribology of electroless nickel coatings: a review. Mater Des 32:1760–1775
24. Sudagar J, Lian J, Sha W (2013) Electroless nickel, alloy, composite and nano coatings: a critical review. J Alloy Compd 571:183–204

25. Rocha SSD, Adabo GL, Henriques GEP, Nobilo MADA (2006) Vickers hardness of cast commercially pure titanium and Ti-6Al-4V alloy sumitted to heat treatments. Braz Dent J 17:126–129

26. Ciubotariu AC, Benea L, Varsanyi ML, Dragan V (2008) Electrochemical impedance spectroscopy and corrosion behaviour of Al_2O_3–Ni nano composite coatings. Electrochim Acta 53:4557–4563

27. Mohammed ES, Martha ES, Helge FB (2005) Assessing the biocompatibility of NiTi shape memory alloys used for medical applications. Anal Bioanal Chem 381:557–567

28. Fayyad EM, Hassan MK, Rasool K, Mahmoud KA, Mohamed AMA, Jarjoura G, Farhat Z, Abdullah AM (2019) Novel electroless deposited corrosion-resistant and anti-bacterial NiP–TiNi nanocomposite coatings. Surf Coat Technol 369:323–333

29. Mazaheri H, Allahkaram SR (2012) Characterization and electrochemical evaluation of Ni–P-nano diamond composite coatings. Appl Surf Sci 258:4574–4580

30. Islam MA, Farhat ZN (2015) Mechanical and electrochemical synergism of API X42 pipeline steel during erosion-corrosion. J Bio Tribo Corros 1:1–18

31. Islam MA, Farhat ZN, Ahmed EM, Alfantazi AM (2013) Erosion enhanced corrosion and corrosion enhanced erosion of API X-70 pipeline steel. Wear 302:1592–1601

32. Jang JSC, Chang YS, Li TH, Hsieh PJ, Huang JC, Tsao CYA (2010) Plasticity enhancement of $Mg_{58}Cu_{28.5}Gd_{11}Ag_{2.5}$ based bulk metallic glass composites dispersion strengthened by Ti particles. J Alloy Compd 504:S102–S105

33. Islam MA, Farhat Z (2017) Erosion–corrosion mechanism and comparison of erosion–corrosion performance of API steels. Wear 376–377:533–541

34. Creus J, Mazille H, Idrissi H (2000) Porosity evaluation of protective coatings onto steel through electrochemical techniques. Surf Coat Technol 130:224–232

35. Lin C, Dadvand N, Farhat Z, Kipouros G (2013) Electroless nickel phosphorous plating on carbon steel. Mater Sci Technol 3:2224–2237

36. Gheshlaghi MG, Seifzadeh D, Shoghi P, Yangjeh AH (2018) Electroless Ni–P/nano-WO_3 coating and its mechanical and corrosion protection properties. J Alloy Compd 769:149–160

37. Qi J, Huang B, Wang Z, Ding H, Xi J, Fu W (2017) Dependence of corrosion resistance on grain boundary characteristics in a high nitrogen CrMn austenitic stainless steel. J Mater Sci Technol 33:1621–1628

38. Diegle RB, Sorensen NR, Clayton CR, Helfand MA, Yu YC (1988) An XPS investigation into the passivity of an amorphous Ni-20P. J Electrochem Soc 135:1085–1092

39. Pourbaix M (1974) Altas of electrochemical equilibria in aqueous solutions. National Association of Corrosion Engineers, Houston, pp 493–450

40. Ching WY (1986) Electronic structures of amorphous $Ni_{1-x}P_x$ glasses. Phys Rev B 34:2080–2087

41. Li K, Li Y, Huang X, Gibson D, Zheng Y, Liu J, Sun L, Fu YQ (2017) Surface microstructures and corrosion resistance of Ni-Ti-Nb shape memory thin films. Appl Surf Sci 414:63–67

42. Aal AA (2008) Hard and corrosion resistant nanocomposite coating for Al alloy. Mater Sci Eng A 474:181–187

43. Mahmud AS, Ng CW, Razali MF (2016) Effect of surface oxidation on shape memory behaviour of NiTi alloy. AIP Conf Proc 1774:1–6

44. Wojcieszak D, Mazur M, Indyka J, Jurkowska A, Kalisz M, Domanowski P, Kaczmarek D, Domaradzki J (2015) Mechanical and structural properties of titanium dioxide deposited by innovative magnetron sputtering process. Mater Sci 33:660–668

45. Chen WW, Gao W (2011) Microstructures and properties of sol-enhanced nanostructured metal-oxide composite coatings. Prog Nat Sci 21:355–362

46. Uysal M (2019) Electroless codeposition of Ni–P composite coatings: effects of graphene and TiO_2 on the morphology, corrosion, and tribological properties. Metall Mater Trans A 50:2331–2341